JOURNAL OF GEOPHYSICAL RESEARCH, VOL. 113, D15S19, doi:10.1029/2007JD008689, 2008

Evaluation of the OMI cloud pressures derived from rotational Raman scattering by comparisons with other satellite data and radiative transfer simulations

Alexander Vasilkov,[1] Joanna Joiner,[2] Robert Spurr,[3] Pawan K. Bhartia,[2] Pieternel Levelt,[4] and Graeme Stephens[5]

Received 22 March 2007; revised 15 October 2007; accepted 29 November 2007; published 9 May 2008.

[1] In this paper we examine differences between cloud pressures retrieved from the Ozone Monitoring Instrument (OMI) using the ultraviolet rotational Raman scattering (RRS) algorithm and those from the thermal infrared (IR) Aqua/MODIS. Several cloud data sets are currently being used in OMI trace gas retrieval algorithms including climatologies based on IR measurements and simultaneous cloud parameters derived from OMI. From a validation perspective, it is important to understand the OMI retrieved cloud parameters and how they differ with those derived from the IR. To this end, we perform radiative transfer calculations to simulate the effects of different geophysical conditions on the OMI RRS cloud pressure retrievals. We also quantify errors related to the use of the Mixed Lambert-Equivalent Reflectivity (MLER) concept as currently implemented of the OMI algorithms. Using properties from the Cloudsat radar and MODIS, we show that radiative transfer calculations support the following: (1) The MLER model is adequate for single-layer optically thick, geometrically thin clouds, but can produce significant errors in estimated cloud pressure for optically thin clouds. (2) In a two-layer cloud, the RRS algorithm may retrieve a cloud pressure that is either between the two cloud decks or even beneath the top of the lower cloud deck because of scattering between the cloud layers; the retrieved pressure depends upon the viewing geometry and the optical depth of the upper cloud deck. (3) Absorbing aerosol in and above a cloud can produce significant errors in the retrieved cloud pressure. (4) The retrieved RRS effective pressure for a deep convective cloud will be significantly higher than the physical cloud top pressure derived with thermal IR.

Citation: Vasilkov, A., J. Joiner, R. Spurr, P. K. Bhartia, P. Levelt, and G. Stephens (2008), Evaluation of the OMI cloud pressures derived from rotational Raman scattering by comparisons with other satellite data and radiative transfer simulations, *J. Geophys. Res.*, *113*, D15S19, doi:10.1029/2007JD008689.

1. Introduction

[2] The Aura Ozone Monitoring Instrument (OMI), alone and in combination with other Aura instruments, has been used to retrieve tropospheric amounts of the U.S. Environmental Protection Agency (EPA) criteria pollutants ozone (O3) (and ozone precursor formaldehyde, HCHO), NO2, SO2, and aerosol at higher spatial resolution than any previous instrument. The full-width half-maximum (FWHM) pixel edges are 14 and 24 km in the along- and across-track directions, respectively, at nadir and 30 by 160 km at the swath edge. More details on the OMI instrument are given by *Levelt et al.* [2006].

[3] Clouds affect every algorithm used to derive information about trace gases and aerosol from OMI. Clouds may be considered a nuisance for some remote sensing applications. However, in the visible (VIS) and ultraviolet (UV), their effects can be accounted for to first order with relatively simple models. Therefore, information about trace gases can be accurately retrieved in their presence.

[4] Cloud pressures are retrieved from the Ozone Monitoring Instrument (OMI) using either atmospheric rotational Raman scattering (RRS) in the UV [*Joiner et al.*, 2004] or oxygen dimer (O2-O2) absorption near 477 nm in the VIS channel [*Acarreta et al.*, 2004]. The RRS algorithm uses a fitting window of 346–354 nm in the UV-2 channel that has an average spectral sampling distance of 0.15 nm and a FWHM slit width of 0.45 nm. Both OMI cloud algorithms are based on the fact that clouds screen the atmosphere below from satellite observations [e.g., *Joiner and Bhartia*, 1995]. Therefore, clouds in general reduce the amount of RRS and absorption seen by satellite-borne instruments.

[1] Science Systems and Applications Incorporated, Lanham, Maryland, USA.
[2] NASA/Goddard Space Flight Center, Greenbelt, Maryland, USA.
[3] RT Solutions Incorporated, Cambridge, Massachusetts, USA.
[4] Royal Netherlands Meteorological Institute (KNMI), De Bilt, Netherlands.
[5] Colorado State University, Fort Collins, Colorado, USA.

0148-0227/08/2007JD008689$09.00

[5] There are ongoing comparisons of cloud pressures from different techniques and instruments in the A-train formation of satellites that fly within approximately 15 min of each other. These include comparisons of cloud pressures from both OMI algorithms, O2-A band from the Polarization and Directionality of the Earth Reflectances (POLDER) instrument flying aboard the Polarization and Anisotropy of Reflectances for Atmospheric Sciences coupled with Observations from a Lidar (PARASOL) satellite, and MODIS thermal infrared (IR) [see, e.g., *Sneep et al.*, 2008]. Similar comparisons have been made with the Global Ozone Monitoring Experiment (GOME) aboard the European Space Agency's Environmental Research Satellite-2 (ERS-2) [e.g., *Vasilkov et al.*, 2004; *Joiner et al.*, 2004; *Koelemeijer et al.*, 2001; *de Beek et al.*, 2001]. Two main findings emerge from these studies: (1) There is generally good agreement between cloud pressures derived from the scattering and absorption techniques especially at high cloud fractions; and (2) Although there is good agreement for many cases between cloud pressures derived from scattering/absorption and those derived from the thermal IR using the CO2 slicing and thermal window techniques [e.g., *Menzel et al.*, 1992], there are some conditions for which significant differences exist.

[6] Here, we show that RRS effects in the UV depend not only on the physical cloud top, but on the vertical distribution of cloud optical depth (e.g., the cloud vertical extent and the optical depths in multiple-layer cloud situations). Without prior knowledge of this information, it is not possible to correctly estimate the physical cloud top even with a perfect radiative transfer model. Therefore, we should not expect optical (UV/VIS) cloud pressures to necessarily agree with cloud top estimates provided by thermal IR techniques. In fact, the combination of optical and thermal IR cloud observations could be used to detect the presence of multiple cloud decks and may ultimately yield information about cloud vertical extent. We have therefore taken a different approach to evaluate the retrieved cloud pressures. The addition of the Cloud Profiling Radar (CPR) on CloudSat [*Stephens et al.*, 2002] to the A-train provides new insight into optical and thermal IR cloud pressure differences. The CPR generates simultaneous 2-D radar reflectivity cross sections through clouds. The combination of information from CPR and MODIS yields estimates of vertical optical depth profiles. We use these profiles with a radiative transfer model to simulate OMI observations. We then retrieve a cloud pressure with the simulated data and compare with the actual OMI retrievals in a closure experiment. We focus here on a tropical deep convective system that includes both vertically extended clouds and distinct two-layer cloud situations.

[7] We also examine errors in the retrieved cloud pressure due to the use of the Mixed Lambert-Equivalent reflectivity (MLER) model. The MLER concept is currently used in all other OMI trace gas retrieval algorithms including those for total column ozone. *Koelemeijer and Stammes* [1999] showed the importance of using accurate cloud pressures for retrieving total column ozone. In order to continue the long time record of TOMS observations with a consistent algorithm, the TOMS-based (TOMS-V8) OMI (OMTO3) total column ozone algorithm [*Bhartia and Wellemeyer*, 2002; *McPeters et al.*, 2008] uses a cloud pressure climatology that is based on thermal IR satellite data. *Vasilkov et al.* [2004] showed that the use of simultaneously derived cloud pressures from RRS in place of climatological cloud pressures improves the retrieval of ozone above clouds in the TOMS-V8 algorithm. *Joiner et al.* [2006] also found that total column ozone within hurricane eyes may be significantly overestimated by TOMS-V8 when climatological cloud pressures are used.

[8] Accurate cloud pressures are also needed to study long-term and seasonal variations in tropical tropospheric ozone derived from cloud slicing technique [*Ziemke et al.*, 2001]. This method makes use of variations in the measured column values owing to differences in cloud pressure to derive an average mixing ratio over the pressures spanned. This method has been implemented with TOMS using IR-derived cloud top pressures, but has more recently been applied to OMI using the more applicable cloud pressure derived from the OMI RRS algorithm (J. Ziemke, private communication, 2007). Tropospheric ozone has also been estimated from the residual methods, e.g., using total ozone from the OMI TOMS-V8 and stratospheric ozone from the Aura Microwave Limb Sounder (MLS) [e.g., *Ziemke et al.*, 2006]. The use of retrieved cloud pressures from visible/UV retrievals may improve the tropospheric ozone derived by these methods.

[9] The paper is structured as follows. In section 2, we briefly describe the RRS operational cloud pressure algorithm referred to as OMCLDRR and updates made since the initial release. In section 3 we show comparisons of the OMI cloud pressures with other satellite data for different geophysical situations. Section 3 also presents results of radiative transfer (RT) simulations. This includes an evaluation of the MLER performance for various types of clouds and viewing geometries, the effects of errors in the assumed surface albedo, the sensitivity of the algorithm to the geometrical cloud thickness and specific geophysical scenarios such as two-layer clouds, deep convective clouds, and absorbing aerosol above/below a cloud. Conclusions and suggestions for future work are given in the last section.

2. Operational RRS Algorithm

2.1. Description

[10] The OMCLDRR algorithm uses the MLER concept that treats a cloud or ground as a horizontally homogeneous opaque Lambertian-reflecting surface. When the effective cloud fraction, f, is between zero and unity, the measured TOA radiance (normalized by the solar flux), I_m, is treated as a weighted sum of the clear sky (or ground) and overcast (cloud) subpixel radiances, I_g and I_c, respectively, i.e.,

$$I_m = I_g(1-f) + I_c f. \tag{1}$$

[11] I_g and I_c are computed assuming Lambertian reflecting surfaces with predefined reflectivities R_g and R_c. The effective cloud fraction is determined from equation (1) using a wavelength with negligible RRS. All results shown in this paper use the assumptions of $R_g = 0.15$ and $R_c = 0.80$ consistent with TOMS-V8. In the OMCLDRR data set, these products are named CloudPressureforO3 and CloudFractionforO3.

[12] The OMCLDRR algorithm retrieves an effective cloud pressure from the measured amount of filling-in and

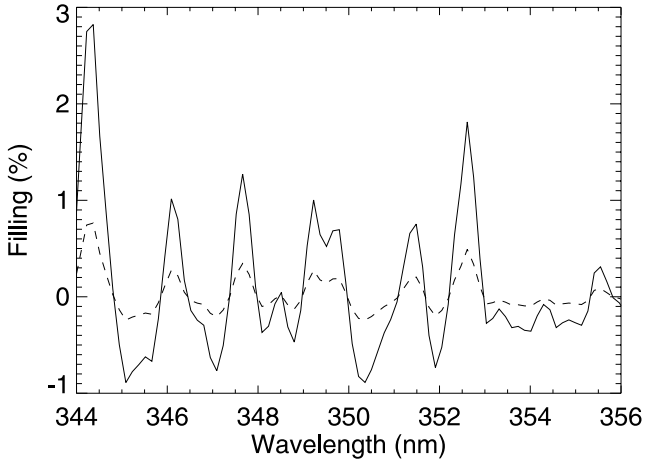

Figure 1. Rotational Raman scattering (RRS) filling-in computed for a Lambertian surface with albedo of 0.6 placed at 700 hPa (solid line) and 200 hPa (dashed line). Observation is at nadir and solar zenith angle of 45°.

depletion of solar Fraunhofer lines caused by RRS. The filling-in effect results in a high-frequency structure in the top-of-the-atmosphere (TOA) radiance spectrum. The effective cloud pressure, p, is derived by a minimum-variance technique that spectrally fits the observed high-frequency structure of TOA reflectance, I_{TOA}. Figure 1 shows an example of the calculated RRS filling-in within the OMCLDRR fitting window for two different cloud pressures. The RRS filling-in is defined as a percentage ratio of the inelastic RRS component of the TOA radiance to the elastically scattered component.

[13] We model the TOA reflectance as a sum of a spectrally linear component accounting for Raleigh and aerosol scattering and a high-frequency component accounting for RRS denoted by r, i.e.,

$$I_{\mathrm{TOA}} = A + B\lambda + r\left(p, \lambda, R_c, R_g, f, \theta, \theta_0, \varphi\right), \qquad (2)$$

where λ is wavelength, A and B are coefficients to account for the linear spectral dependence, θ is the viewing zenith angle, θ_0 is the solar zenith angle, and φ is the relative azimuth angle. The RRS component is calculated using the approach of *Joiner et al.* [1995, 2004].

2.2. Wavelength Fitting Window

[14] The first released version of the OMCLDRR algorithm (v1.0.2) employed a fitting window in the OMI VIS channel that included the deep Ca Fraunhofer H and K lines (392–398 nm). Initial evaluation of this version revealed that the retrieved cloud pressures were too low in some partly cloudy conditions. This may result from non-Lambertian behavior of the Earth's surface and clouds as well as cloud shadowing. OMCLDRR is particularly sensitive to such effects because light directly transmitted through the atmosphere undergoes no Raman scattering. Therefore, any increase in the directly transmitted component of the observed radiance as compared with a Lambertian surface (e.g., in the presence of sea glint) obscures the effects due to Raman scattering. In this situation, OMCLDRR produces cloud pressures that are too low. Note that the OMI O2-O2 cloud pressure algorithm referred as OMCLDO2 and other absorption-based algorithms will have the opposite effect; In the presence of sea glint, the retrieved pressures from an absorption approach will tend toward the surface pressure. Near the swath edges, there is more diffuse light in the TOA reflectance than in the central swath positions. This increase in Rayleigh scattering at the swath edges reduces the contribution of the directly transmitted light and therefore tends to reduce the effects of non-Lambertian surfaces.

[15] The current version (OMCLDRR v1.2.0) utilizes a shorter-wavelength fitting window in the UV-2 channel (345–354 nm). Increased Rayleigh scattering in the UV-2 window mitigates problems with non-Lambertian surfaces and cloud shadowing. In particular, we saw significant improvements over glint-contaminated areas when we moved the fitting window to shorter wavelengths with more Rayleigh scattering. Raman scattering from the ocean is also negligible at these wavelengths whereas it is significant at 395 nm. We calculate oceanic Raman scattering using a climatological chlorophyll database with the model of *Vasilkov et al.* [2002].

[16] Figure 2 shows the difference in cloud pressures derived using the two fitting windows for all orbits on 21 December 2004. There is virtually no difference for bright clouds (scene reflectivity R > 60%). However, the cloud pressures can be significantly different in the partially cloudy scenes (e.g., 30% < R < 50%) especially at the center of the swath. The cloud pressures from the 395 nm window are almost always lower than those from the 350 nm window. For reference, the cloud pressures from the 350 nm window are shown in Figure 3. Over snow and ice, the cloud fraction is set to unity and the retrieved pressure indicates an effective scene pressure. Therefore, over high-latitude pixels covered by snow and ice with very thin or no clouds, the retrieved pressures should be equal to the surface pressure. The soft calibration procedure described by *Joiner and Vasilkov* [2006] uses this property to minimize along-track biases (striping) in the OMCLDRR cloud pressure product.

3. RT Simulations and Comparisons With Other Satellite Data

[17] In this section, we simulate OMI radiances including both elastic and inelastic scattering. We then present those forward calculations to a simplified retrieval algorithm in order to obtain a better understanding of how the algorithm reacts to various situations. In particular, we focus on the effects of (1) cloud geometrical thickness, (2) the MLER approximation, (3) errors in the surface albedo assumption, (4) aerosol in, above, and below clouds, (5) distinct multiple cloud decks, and (6) deep convective clouds. Comparisons with other satellite data are shown for the latter three scenarios. We first provide a detailed account of the forward and inverse calculations.

3.1. LIDORT-RRS Forward Model

[18] To calculate inelastic RRS to all orders in a multiple scattering medium, we would require radiances to be calculated at all wavelengths simultaneously. Since RRS is small (~4% of Rayleigh), we treat it as a perturbation

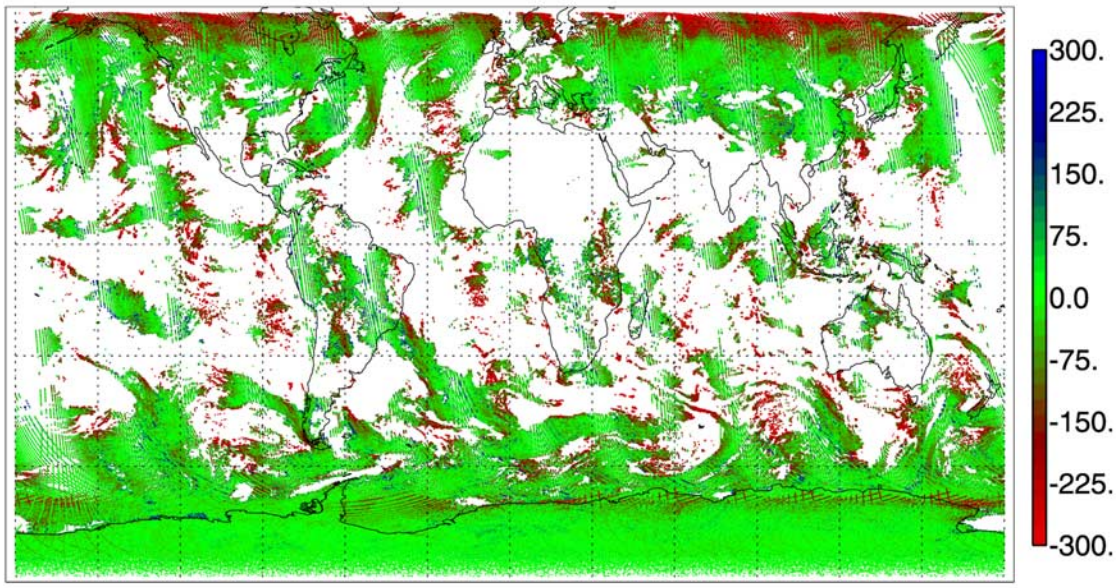

Figure 2. Cloud pressures (hPa) retrieved with 395 nm fitting window minus those retrieved with 350 nm window for effective cloud fraction $f > 0.2$ on 21 December 2004. Each Ozone Monitoring Instrument (OMI) pixel is shown as a dot (i.e., this representation does not account for differing pixel sizes). White indicates areas with either missing data or $f < 0.2$.

effect. At zero order (no RRS, elastic scattering), radiances are computed with molecular scattering described by the Rayleigh phase function and cross section. With first-order RRS, we consider photons that are Raman scattered once only into and out of a given wavelength λ. Source terms will include primary scattering (elastic and inelastic) of the direct solar beam. For multiply scattered light, we assume that diffuse fields at λ and all Raman-shifted redistribution wavelengths have first been determined using zero-order elastic RT calculations before undergoing the first Raman scatter. In this case, the radiative transfer equation (RTE) can then be solved in the usual manner, but with a number of additional source terms due to Raman scattering of the direct beam and first-order Raman scattering of an elastically scattered diffuse field. A similar perturbation approach has been used previously [*Vountas et al.*, 1998; *Landgraf et al.*, 2004].

[19] The Linearized Discrete-Ordinate Radiative Transfer (LIDORT)-RRS model [*Spurr et al.*, 2008] is a new multiple scattering model with first-order RRS source terms. The discrete ordinate methodology is similar that for the LIDORT radiative transfer model [*Spurr et al.*, 2001; *Spurr*, 2002]. The radiation field is expressed as a Fourier cosine series in the relative azimuth between solar and viewing

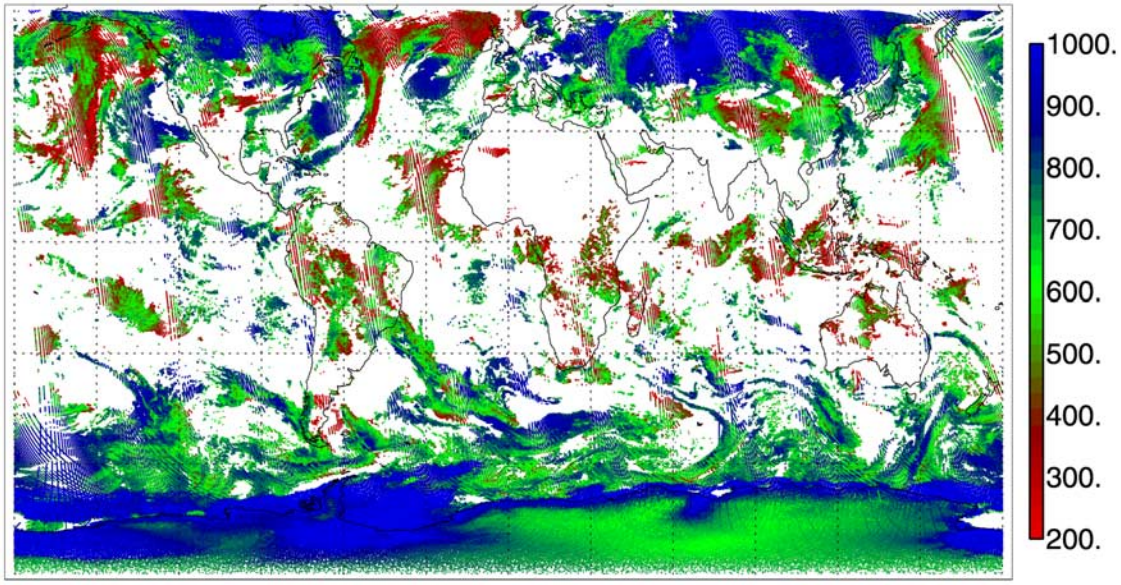

Figure 3. As in Figure 2, but showing the effective cloud pressure (hPa) retrieved with 350 nm window.

directions. Because of the $\cos^2\gamma$ scattering-angle dependence of the Raman phase function, only the Fourier components $m = 0$, 1 and 2 will contain RRS contributions. Homogeneous solutions to the RTE (in the absence of sources) are found by eigenvalue methods. Particular integrals for the zero-order field are written in the form $I(m, \tau) = W(m)\exp[-\tau/m_0]$, where τ is the optical depth and m_0 the solar zenith angle cosine in a plane-parallel medium. For the RTE with RRS sources, it is necessary to use Green's function methods [*Siewert*, 2000; *Spurr*, 2002] to determine the particular integrals in a consistent manner. Radiative transfer "post processing" (determination of radiance at arbitrary polar angle and optical depth) is done by source function integration. Note that the diffuse elastic field at Raman-shifted wavelengths needs to be determined only at discrete ordinate directions. Post processing is confined to the inelastic RT solution.

[20] LIDORT-RRS has most of the capabilities of the regular LIDORT code. There are output options for upwelling and/or downwelling backscatter radiances at arbitrary geometry and atmospheric optical depth. The delta-M scaling approximation is used to deal with phase functions with strong forward (elastic) scattering. There is also an implementation of the Nakajima-Tanaka correction procedure for correcting the elastic single scatter contribution. At present, the model assumes a Lambertian surface for the lower boundary condition, but this is easily generalized to a full anisotropic treatment. The LIDORT-RRS model does not currently include polarization. A vector version of the code is currently under development.

[21] Raman spectroscopic data in LIDORT-RRS is taken from *Chance and Spurr* [1997]. There are 233 Raman transitions in this data set. A complete calculation requires elastic-scattering diffuse-field RT simulations to be performed at all Raman-shifted wavelengths. In addition to the full monochromatic mode, LIDORT-RRS has a fast mode of operation called the "binning realization," in which RT calculations are done only at the wavelengths of the input solar spectrum. In this realization, Raman transitions are grouped into wavelength bins defined by the solar spectrum. The binning realization is suitable for moderate-resolution instruments such as OMI and GOME (see *Spurr et al.* [2008] for details).

[22] In our model, the atmosphere is divided into a number of optically uniform layers, and it can include any number of particulates (aerosols and clouds, scattering elastically) in addition to Rayleigh and Raman molecular scattering and trace gas absorption. One of the advantages of the LIDORT-RRS model is its ability to deal comfortably with optically thick cloud layers. In contrast, the successive orders of scattering model [*Joiner et al.*, 1995] is applicable to molecular scattering and contains no aerosol treatment. The calculated filling-in from LIDORT-RRS agrees well with that from *Joiner et al.* [1995] in a cloud free atmosphere [*Spurr et al.*, 2008].

3.2. LIDORT Forward Model Environment

[23] LIDORT-RRS is a pure scattering code, and it can be considered as a generic model for computing elastic and inelastic components of the radiances. Here, we provide details of input optical properties needed for our specific RT calculations. For the first series of calculations, we used a plane-parallel cloud of 1 km geometric thickness, with cloud optical depths, τ, between 5 and 50. The Henyey-Greenstein (H-G) phase function with the asymmetry factor $g = 0.85$ was used to model the angular distribution of cloud scattering. The cloud single scattering albedo was set to unity. For consistency with the MLER model used in the operational cloud pressure algorithm, the surface albedo was assumed to be equal to 0.15. Additional simulations were done with surface albedo 0.05 to study the effects of errors in our MLER-assumed reflectivity of 0.15. The surface pressure was set to 1013 hPa. All simulations use the OMI measured solar irradiance to compute the filling-in due to RRS.

3.3. Simplified Inverse Model: Cloud Pressure Retrieval From OMI Synthetic Data

[24] Cloud pressure is retrieved from the simulated data using a simplified version of the operational algorithm. Instead of fitting multiple Fraunhofer lines within a spectral window, we use a single wavelength (352.6 nm, the center of the strongest line within the spectral fitting window). A basic formulation follows equation (1) with explicit RRS terms:

$$I_s(1+k) = I_g\big(1+k_g\big)(1-f) + I_c(1+k_c)f, \tag{3}$$

where I_s is the simulated elastic radiance and k is the filling-in factor with subscripts g and c for the ground and cloud components respectively. The filling-in factor is defined as

$$k = (I_t - I_e)/I_e, \tag{4}$$

where I_t is the total radiance and I_e is the elastic radiance. Radiances are assumed to be normalized by the incoming solar irradiance throughout. The cloud fraction is determined at a reference wavelength, $\lambda_0 = 354.1$ nm, where the RRS effect is negligible, i.e.,

$$\begin{aligned} I_s(\lambda_0) =& I_g\big(R_g = 0.15, p_g = 1013\ \text{hPa}\big)(1-f) \\ &+ I_c(R_c = 0.80, p_c = 700\ \text{hPa})f. \end{aligned} \tag{5}$$

[25] In equation (5), the cloud radiance, I_c, is calculated for an opaque Lambertian-reflecting surface with reflectance of 80% at a reference pressure of 700 hPa. The cloud radiance does not depend significantly on the reference pressure.

[26] For $0 < f < 1$, the MLER cloud pressure is determined as follows. At a wavelength of the center of the strongest Fraunhofer line, equations (3), (4), and (5) can be combined to give

$$I_s k = I_g k_g (1-f) + I_c k_c f. \tag{6}$$

[27] The inelastic contribution from the cloudy portion of the scene is therefore given by

$$I_c k_c = \big[I_s k - I_g k_g (1-f)\big]/f. \tag{7}$$

[28] Cloud pressure is determined by interpolating a lookup table generated for the inelastic scattering radiance $I_c k_c$. The inelastic scattering radiances are precomputed for

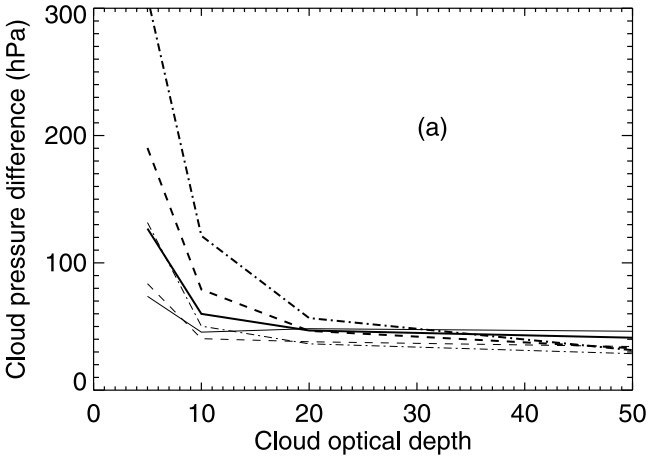

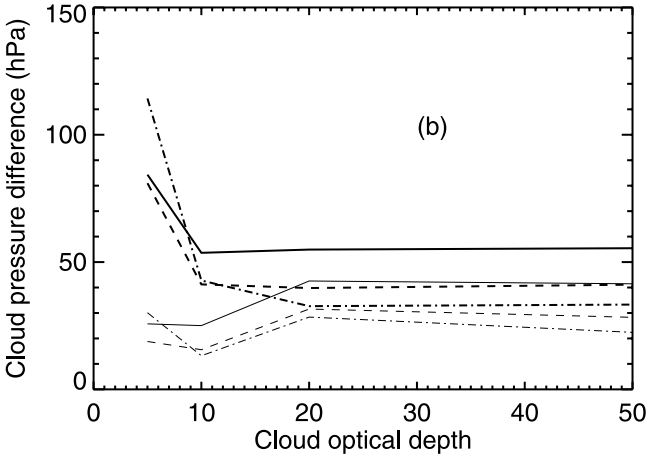

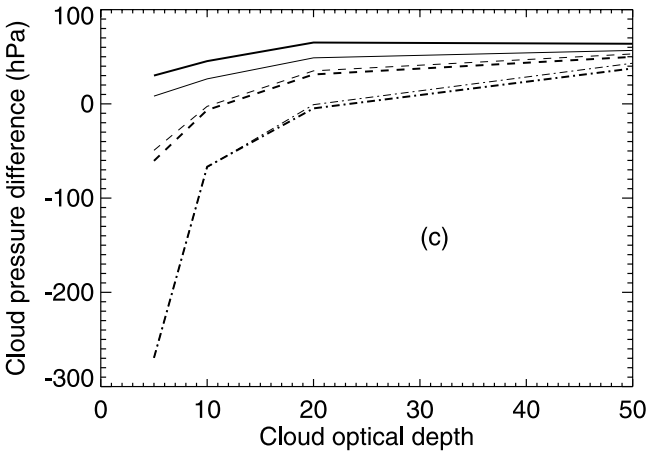

Figure 4. (a) Cloud pressure errors as a function of cloud optical depth τ at SZA = 20°. (thick lines) Observations at nadir; (thin lines) VZA = 40° and azimuth angle of 90°; (solid lines) true cloud top height of 798 hPa (2 km); (dashed lines) 476 hPa (6 km); (dash-dot lines) 270 hPa (10 km). (b) Cloud pressure errors as a function of cloud optical depth τ at SZA = 45°. (c) Cloud pressure errors as a function of cloud optical depth τ at SZA = 70°.

opaque Lambertian-reflecting surfaces with reflectance of 80% placed at a set of cloud pressures.

[29] Cloud fraction determined from equation (5) depends on assumed surface and cloud albedos and may appear to be greater than unity if $I_s(\lambda_0) > I_c$. If $f > 1$, cloud fraction is set to unity and the cloud (or scene) pressure is determined using the scene reflectivity. This scenario is referred to as the LER model (i.e., no mixture of clear and cloudy components). The scene reflectivity, R, is calculated at the reference wavelength, λ_0 assuming a Lambertian surface, i.e.,

$$I_s = I_c = I_0 + RFT/(1 - RS_b), \tag{8}$$

where I_0 is the radiance calculated for $R = 0$, F is the total irradiance reaching the surface, T is the transmittance of the radiance reflected from the surface, and S_b is the fraction of the reflected surface radiance that is scattered by the atmosphere back to the surface. Then, assuming R is wavelength independent, cloud pressure is determined from a lookup table for the inelastic scattering radiance, $I_c k_c$, at the computed scene reflectivity.

3.4. Estimates of MLER Errors

[30] Figure 4 shows differences between the retrieved cloud pressure and true (simulated for the overcast case) cloud top pressure as a function of τ for various solar zenith angles (SZA) and cloud pressures. We find relatively small errors (within ~50 hPa) due to the MLER assumption for clouds with $\tau > 10$ with little dependence on cloud pressure. Under these conditions, the calculated RRS contribution from the clear sky subpixel correctly accounts for that from the light backscattered from within and below the cloud. For optically thinner clouds, errors may be significantly larger (both positive and negative) and depend on cloud height, SZA, and τ. The errors are smallest for SZA = 45° (Figure 4b). At SZA = 70° and a cloud pressure of 270 hPa (10 km), the term $I_c\ k_c$ of equation (6) decreases with τ and approaches zero at optical depths $\tau \sim 5$ which in turn leads to a retrieved cloud pressure of zero. The opposite effect takes place at low SZA (Figure 4a). The error dependence on viewing zenith angle (VZA) is significant only for low SZA and τ.

3.5. Estimates of Surface Albedo Errors

[31] Figure 5 shows errors in retrieved cloud pressures when radiances were simulated with a surface albedo of 0.05 at SZA = 45°. As stated above, the MLER model as implemented in OMCLDRR assumes a ground reflectivity of 0.15. For optically thick clouds ($\tau > 10$), the errors are similar to those produced with a surface albedo of 0.15. However, the mismatch between actual and assumed surface albedo results in significant cloud pressures errors for optically thin high-altitude clouds. The ground reflectivity of 0.15 was chosen to be consistent with the assumption of the TOMS-V8 algorithm. This relatively high value of ground reflectivity was selected to account for aerosol and small amounts of cloud contamination. When the actual reflectivity of ground is less than this value, however, the OMCLDRR cloud pressure error increases.

[32] Figures 6 and 7 show a CloudSat CPR reflectivity cross section along with collocated OMI cloud pressures and corresponding effective cloud fractions from both the

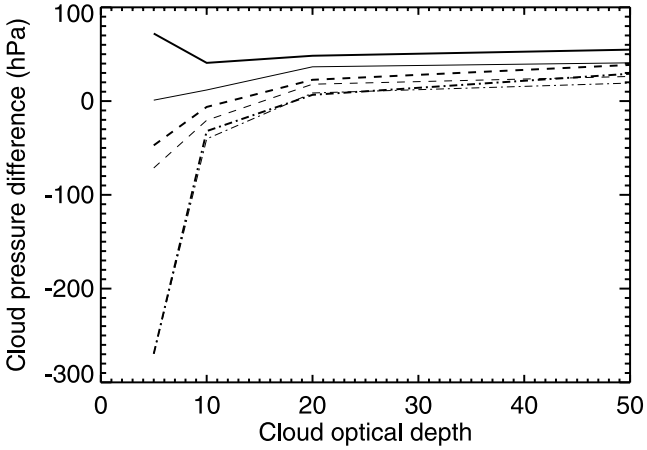

Figure 5. As in Figure 4, but showing cloud pressure errors resulting from a surface albedo error of 0.1 at SZA = 45°.

OMCLDRR and OMCLDO2 algorithms. Figures 6 and 7 show OMCLDRR retrievals that assumed surface albedos of 0.15 and 0.05, respectively. This track is from 13 November 2006 over a cloudy region of the Southern Pacific ocean and corresponds to Cloudsat granule 2906 and OMI orbit 12402. The overall agreement between the two OMI cloud algorithms is excellent when the cloud fractions are high (>50%). The cloud pressures and effective cloud fractions produced with the 0.05 surface albedo, a value close to the TOMS climatology for this location, are closer to those of the OMI O2-O2 cloud algorithm, particularly north of 45°S where the cloud fractions drop below 40%. In the next release of OMCLDRR, we will use a ground reflectivity climatology derived from TOMS in place of the current fixed value. In addition, changes in the OMI calibration will bring the reflectances up in the OMCLDRR fitting window by a few percent in collection 3. This will further increase the retrieved effective cloud fractions, bringing them into closer agreement with those of OMCLDO2. We discuss other aspects of Figure 7 in the next two subsections.

3.6. Sensitivity to Geometrical Cloud Thickness

[33] In the previous subsection, the cloud geometrical thickness was relatively small (1 km). In this subsection, we conduct simulations where we varied the geometrical thickness but kept the total cloud optical depth constant (i.e., we vary the optical depth per unit length). Figure 8 shows how the retrieved cloud pressure, which is approximately proportional to the RRS filling-in at the given geometry, varies with the cloud geometrical thickness. At nadir and SZA = 45°, the retrieved pressure of a hypothetical cloud of uniform optical thickness is slightly less than the cloud pressure midpoint. However, at larger view angles (and SZA), the light does not penetrate as deeply as in the nadir observations so that the retrieved pressure becomes closer to the cloud top pressure than the nadir observation. The results of this simulation are consistent with those of *Ahmad et al.* [2004] who showed significant photon penetration into a hypothetical geometrically thick cloud of uniform optical thickness.

[34] In a case such as this, the pressure retrieved from the thermal IR using a CO2 slicing type algorithm, such as the one implemented for MODIS, would be near the physical cloud top. This simulation therefore demonstrates that UV/VIS scattering/absorption algorithms provide a piece of information that is independent of the cloud top provided by the thermal IR. We should therefore not expect UV/VIS cloud pressures to be the same as those from the IR. As a consequence, it is not appropriate to use thermal IR-derived cloud top pressure to validate UV/VIS cloud pressures. An illustration is shown in Figure 7. The two OMI cloud algorithms consistently retrieve pressures inside vertically

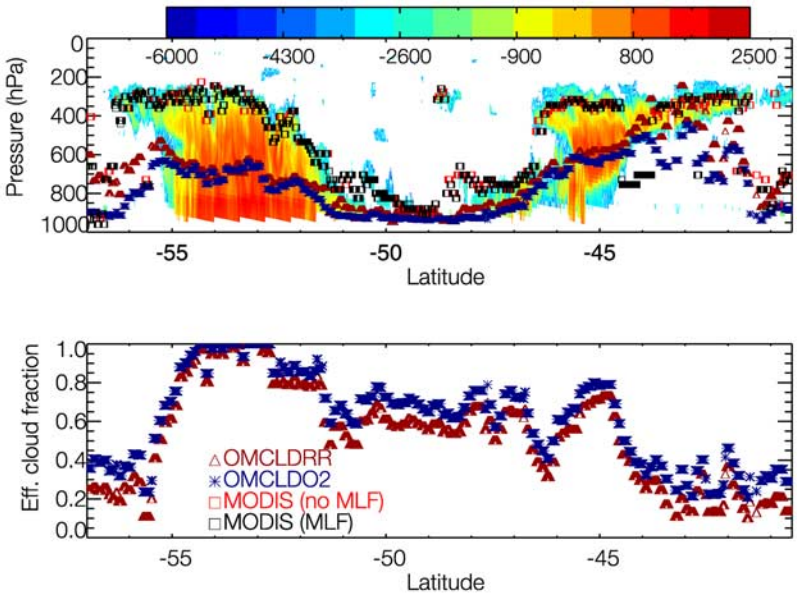

Figure 6. (top) CloudSat CPR reflectivity profiles (arbitrary scale) with collocated OMI (both algorithms, collection 2) and MODIS cloud pressures. (bottom) MLER effective cloud fractions from both OMI algorithms. MODIS data are shown with and without multilayer/phase flag (MLF) set.

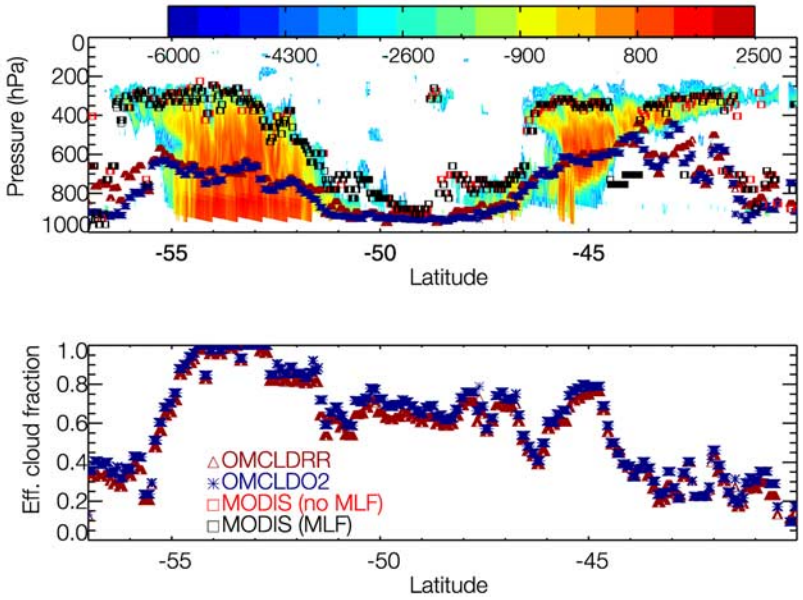

Figure 7. As in Figure 6, but for retrievals that use an assumed surface reflectivity of 0.05.

extended clouds between 52 and 55°S, whereas MODIS retrieves pressures near the physical cloud top. This type of situation will be further explored in section 3.9 in a tropical convective system. Furthermore, UV/VIS cloud pressures are more appropriate for use in UV/VIS trace gas retrieval algorithms that use the MLER model, because they more accurately represent the photon path. This has been recently verified by comparing ozone retrieved with the OMI V8-TOMS algorithm using MODIS and OMI cloud pressures (D. Haffner, private communication, 2007). In the tropics, where the stratospheric and total column ozone variability is relatively small, the total column ozone standard deviation was significantly reduced using both of the OMI cloud products as compared with collocated Aqua MODIS cloud top pressures.

3.7. Two-Layer Cloud

[35] In this subsection, we now perform a simulation for scenarios of nonuniform cloud optical depths. An example of this is a frequently observed situation of two cloud decks. Here, we simulate radiances in a two-layer cloud consisting of the lower layer located at 798 hPa (2 km) and upper layer at 270 hPa (10 km) giving a pressure difference of 528 hPa. The cloud layers are 1 km thick. We set τ = 10 for the lower-layer cloud and varied τ for the upper layer. Retrieved cloud pressures are compared with true cloud top pressures of both the lower and upper layer in Figure 9. For small values of τ for the upper layer, OMCLDRR can retrieve a cloud pressure that is up to 200 hPa larger than the lower-layer cloud top pressure (left y axis of Figure 9). This is due to enhanced filling-in of Fraunhofer lines at low and

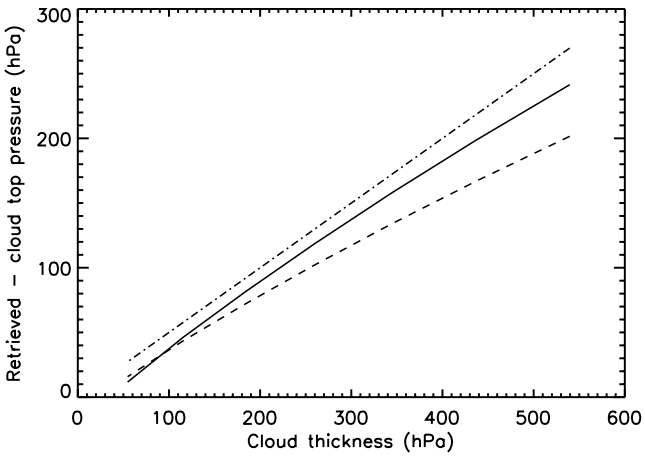

Figure 8. The simulated sensitivity of the retrieved cloud pressure (as measured from the top of the cloud) to the cloud geometrical thickness. (solid line) VZA = 0°; (dashed line) VZA = 40°, azimuth angle = 40°. Dash-dot line represents the cloud pressure midpoint.

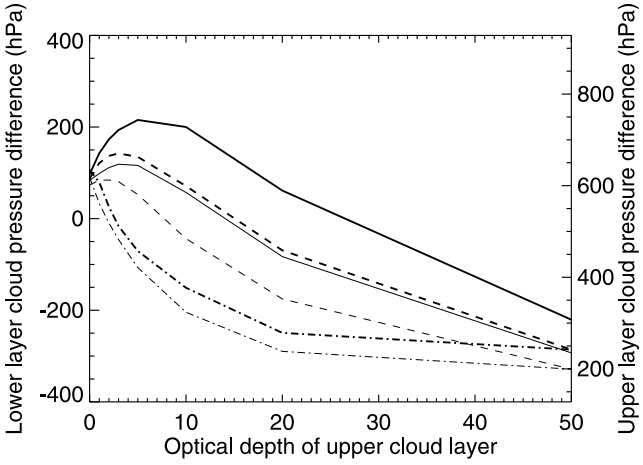

Figure 9. Differences between the MLER cloud pressures and true cloud top pressure of the lower (left-hand axis) and upper (right-hand axis) layers. (thick lines) Nadir; (thin lines) VZA = 40° and azimuth angle of 90°; (solid lines) SZA = 20°; (dashed lines) SZA = 45°; (dash-dot lines) SZA = 70°.

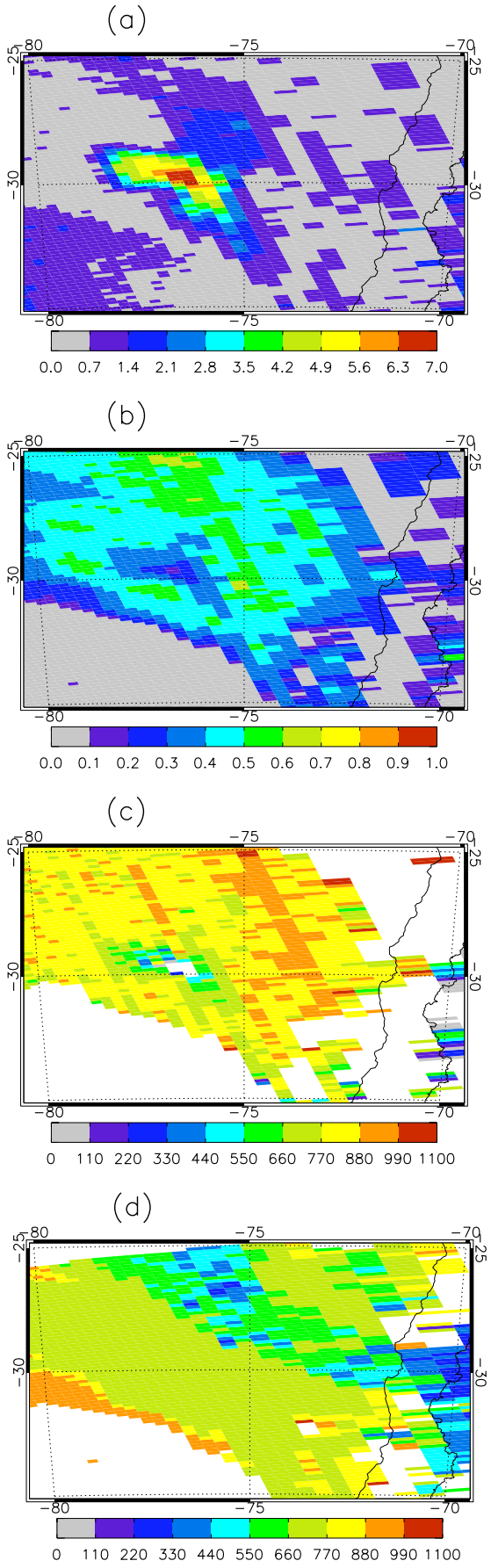

middle SZAs from light that penetrates through the optically thin upper layer and undergoes enhanced scattering between the cloud layers. The range of optical depths of the upper layer at which the effect takes place is typical of cirrus clouds. For high SZA, enhanced filling-in does not occur because of the increase in diffuse light.

[36] When $\tau > 30$ for the upper layer, light penetrates only slightly through the upper layer. The lower cloud deck then contributes a relatively small portion of the observed filling-in. As a result, the RRS cloud pressure algorithm retrieves cloud pressure that is somewhat larger than upper-layer cloud top pressure (right y axis of Figure 9). As τ increases, the retrieved pressure tends toward the upper level cloud top pressure. A variety of different two-layer cloud situations is shown in Figure 7 north of 45°S where scattered low-level clouds are present below an upper layer that decreases in optical depth as latitudes progress northward. When the upper layer is optically thick (near 46°S), OMI cloud pressures are near the bottom of the upper deck. As the upper deck becomes optically thin, the OMI cloud pressures tend toward the pressure of the lower layer.

3.8. Absorbing Aerosol Above/Below Cloud

[37] The UV aerosol index (AI) is a good indicator of the presence of absorbing aerosols [*Herman et al.*, 1997]. Sometimes, a plume of absorbing aerosol is observed in or above clouds. In such cases, OMCLDRR cloud pressures can be significantly lower than MODIS cloud top pressures. Figure 10 shows such an example over the Pacific ocean off the west coast of Chile on 14 January 2007 (OMI orbit/granule 13303). Here, we show maps of the AI, OMCLDRR reflectivity at 354.1 nm, OMCLDRR cloud pressure, and MODIS Collection 5 cloud top pressure averaged over the OMI pixels. The extremely high values of AI (Figure 10a) indicate the presence of absorbing aerosol presumably transported from desert regions of South America. The aerosol plume, brownish in color, was also apparent in MODIS visible imagery (not shown).

[38] MODIS shows a relatively homogeneous horizontal distribution of cloud top pressure in the region of elevated AI values (Figure 10d). According to MODIS, optical depth for clouds in this vicinity is greater than 10. Such high values of optical depth would normally result in an OMCLDRR reflectivity of approximately 0.4 or higher. However, OMCLDRR reports reflectivity values in the range of 0.2–0.4 (Figure 10b) in the region of high AI, with higher values in the surrounding area of low AI. A few pixels have a reflectivity of less than 0.2 indicating the obvious effect of absorbing aerosol above cloud. There is also a pronounced effect of absorbing aerosol on the retrieved cloud pressures. The spatial distribution of the OMI cloud pressures in this region is complex. Most pixels have cloud pressures that are lower than the MODIS cloud top pressures in this region. Note that pixels with cloud fraction < 0.05 are not depicted on the map of OMI

Figure 10. (a) Map of aerosol index on 14 January 2007. (b) Map of reflectivity at 354.1 nm. (c) Map of OMI cloud pressure. (d) Map of MODIS cloud top pressure collocated to OMI pixels.

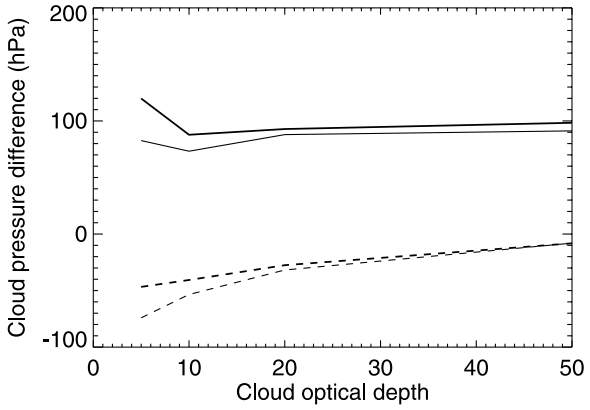

Figure 11. Differences between the MLER cloud pressures and true cloud top pressures as a function of cloud optical depth at SZA = 45°. (solid lines) No aerosol; (dashed lines) absorbing aerosol; (thick lines) observations at nadir; (thin lines) VZA = 40° and azimuth angle of 90°.

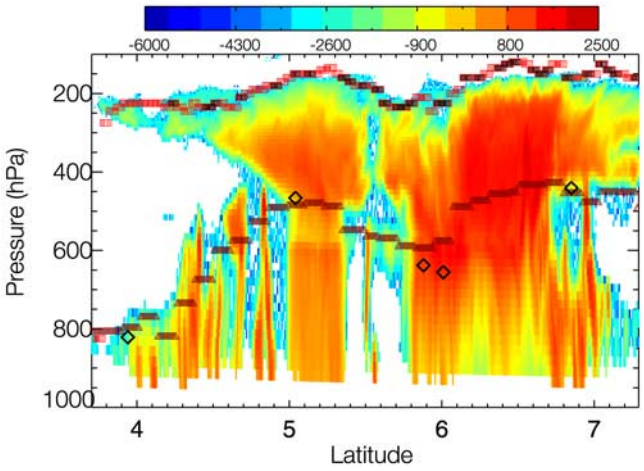

Figure 12. Cloudsat radar reflectivity on 13 November 2006 with cloud pressures retrieved from OMCLDRR (rust triangles), retrieved from MODIS (red squares), and simulated for OMI on the basis of CloudSat/MODIS data (black diamonds).

cloud pressures (Figure 10c) because OMCLDRR does not attempt retrievals for these conditions.

[39] We next simulated the effects of aerosol on OMCLDRR for similar conditions. We generated radiances using plane-parallel cloud located at ~750 hPa with a vertically homogeneous layer of absorbing aerosol (geometrical thickness of 1 km) placed either just below or above the cloud. The aerosol layer was assigned an optical depth of 1.0 and a single scattering albedo of 0.9. We used the H-G phase function with $g = 0.7$ for aerosol. We set the surface albedo to 0.05 and retrieved cloud pressures with the MLER model assuming $R_g = 0.05$. Figure 11 shows that absorbing aerosol above the cloud can reduce the retrieved cloud pressure by approximately 100 hPa for clouds with $\tau > 10$ and up to 200 hPa for clouds with $\tau < 10$. Absorbing aerosol below the cloud has virtually no effect (changes the retrieved cloud pressure by <10 hPa) for clouds with $\tau > 5$. The major effect of the aerosol above a cloud with moderate to high optical depth is to lower the observed reflectance. Then OMCLDRR infers an incorrect lower effective cloud fraction, which in turn leads to retrieved cloud pressures that are too low. Therefore, details of the aerosol layer, such as height above cloud and geometrical thickness, have only a second-order effect on OMCLDRR for such clouds while the absorption optical depth has a first-order effect.

3.9. Closure Calculation in a Tropical Deep Convective Cloud

[40] Figure 12 shows Cloudsat CPR reflectivities in a deep convective cloud in the tropical Pacific on 13 November 2006 (same orbit as shown above in Figure 6). Also shown are MODIS level 2 collection 5 retrieved cloud top pressures [*Platnick et al.*, 2003] (squares near the top of the cloud) and OMCLDRR retrieved effective cloud pressures (rust-colored diamonds inside the cloud). The OMI cloud pressure for a single pixel is represented as a linear segment in order to illustrate the size of the OMI pixel as compared with the higher resolution of CloudSat and MODIS. We also simulated the filling-in for several OMI pixels using the LIDORT-RRS code and optical depth profiles derived with CPR reflectivities [*Stephens et al.*, 2002] and MODIS optical depths. Five profiles of optical depth per km are shown in Figure 13. Values are reported every 0.24 km which yields approximately 60 layers with thicknesses that vary between ~7 and 25 mb. We then presented the simulated data to the simplified retrieval algorithm as described above in order to produce a "simulated" cloud pressure. The simulated results for the five different profiles are shown in Figure 12 as black diamonds. Table 1 provides the tabulated results along with the actual retrieved OMCLDRR reflectivity and that simulated using Cloudsat/MODIS data, the total τ that comes from MODIS, and the τ above and below 550 hPa roughly denoting the separation between ice and liquid water regimes in the cloud. The simulated reflectivities are highly correlated with the actual retrieved values, but are slightly higher on average. The OMI radiometric calibration adjustment that will be applied to the collection 3 data increases the reflectances by ~3% which will bring the observed reflec-

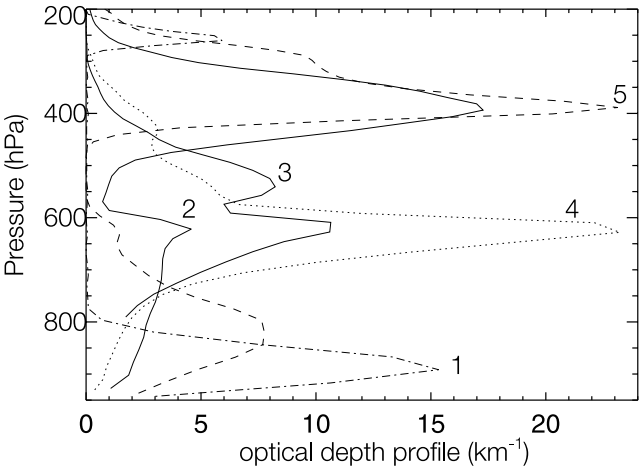

Figure 13. Optical depths per kilometer derived with combined Cloudsat radar and MODIS data. Profiles are numbered as in Table 1.

Table 1. OMI Pixel Information for Simulations[a]

Index	Latitude	Longitude	R_{ret}	R_{sim}	τ_{tot}	τ_{up}	τ_{low}	P_{sim}	P_{ret}
1	4.0	−130.7	0.58	0.68	18.9	5.9	13.0	821	795
2	5.0	−130.9	0.81	0.87	57.1	45.4	11.7	466	483
3	5.9	−131.1	0.74	0.79	31.8	12.9	18.9	638	593
4	6.0	−131.1	0.79	0.82	44.6	11.4	33.2	656	575
5	6.9	−131.3	0.90	0.88	65.9	50.2	15.7	441	452

[a]Latitude, longitude, operational cloud pressure algorithm (OMCLDRR) retrieved (from actual Ozone Monitoring Instrument (OMI) observations) and simulated (from CloudSat/MODIS optical depth profiles) reflectivity (R_{ret}, R_{sim}, respectively), total cloud optical depth (τ_{tot}), cloud optical depth above and below 550 hPa (τ_{up} and τ_{low}, respectively), and retrieved and simulated cloud pressure in hPa (P_{ret} and P_{sim}, respectively).

tivities into closer agreement with the simulations that are based on MODIS cloud optical depths.

[41] Overall, the simulated cloud pressures agree remarkably well with the actual OMCLDRR retrievals. Note that small differences can result from both OMI and Cloudsat retrieval errors and cloud inhomogeneity. Cloudsat provides only a slice through the much larger OMI pixel. MODIS cloud top pressures are always near the physical top of the cloud as defined by the Cloudsat radar reflectivity. However, the OMCLDRR effective cloud pressures are several hundred hPa inside the cloud. These results are consistent with those of *Ahmad et al.* [2004]. They showed, through simulations of ozone absorption in a vertically homogeneous deep convective cloud, that there is significant photon penetration into such a cloud. This produces effective optical cloud pressures that should and do differ significantly with the physical cloud top from the IR. In other words, it would be impossible to estimate the physical cloud top with UV/VIS techniques unless the exact details optical depth profile are known. Cloudsat/MODIS shows that the optical depth profiles are nonuniform and highly variable. The information provided by the UV/VIS can to first order be considered as a radiance-weighted cloud pressure.

[42] OMI captures differences in the vertical cloud profile within the deep convective part of the complex. Lower cloud pressures are retrieved when the optical depths are high in the ice portion of the cloud (profiles 2 and 5). Pressures closer to the optical depth peak in the water portion of the cloud are retrieved when the ice content above is lower (profiles 3 and 4). When two distinct cloud decks are present and the upper deck is optically thin (profile 1 near 4° latitude), the OMCLDRR pressure is near the top or in the middle of the lower cloud deck. However, when the upper cloud deck is optically thick (profile 5 near 7° latitude), the effective pressure is near the bottom of the upper deck. This behavior of OMCLDRR is consistent with the simulations carried out in sections 3.6–3.7.

4. Conclusions and Future Work

[43] Results of our RT simulations, based on both hypothetical clouds and data from CloudSat/MODIS, agree with observations and lead to the following conclusions:

[44] 1. Optical (UV/VIS) cloud pressures depend upon the vertical distribution of cloud optical depth. The effects of RRS as implemented with a MLER model provide a single piece of information in the form of an "optical" cloud pressure that can be considered as a radiance-weighted cloud pressure. The optical cloud pressure is distinct from the physical cloud top that can be retrieved from thermal IR observations and is the appropriate quantity for UV/VIS trace gas algorithms that use the MLER model.

[45] 2. OMCLDRR as currently implemented with the MLER model retrieves cloud pressures in optically thick, geometrically thin clouds that are within ~50 hPa of the physical cloud top for SZA < 70° and VZA < 40°. However, OMCLDRR can have significant cloud pressure errors for optically thin clouds ($\tau < 5$) where the MLER model treats them as broken Lambertian clouds with a small effective cloud fraction.

[46] 3. When the actual reflectivity of the ground is less than that assumed in the MLER model, OMCLDRR underestimates the effective cloud fraction and consequently the cloud pressure, especially for optically thin high-altitude clouds. Because OMCLDRR currently uses a fixed surface albedo that is known to be too high on average, we will incorporate a TOMS-based surface albedo climatology into the next OMCLDRR version.

[47] 4. For the case of optically thin cirrus overlapping an optically thick cloud, OMCLDRR can retrieve cloud pressure that is higher than the lower-layer cloud top pressure at low and moderate SZAs. This is due to enhanced RRS from light that penetrates through the optically thin upper layer and undergoes multiple scattering between the cloud layers. Under other conditions, the retrieved cloud pressure will be in between the pressures of the two decks.

[48] 5. Absorbing aerosol above clouds can reduce the retrieved cloud pressure by several hundred hPa depending on cloud and aerosol optical depths.

[49] 6. Cloudsat radar reflectivities over a deep convective cloud show that MODIS pressures are always near the physical cloud top while the OMCLDRR effective cloud pressures are several hundred hPa inside the cloud. A closure experiment showed that the OMCLDRR-retrieved cloud pressures agree remarkably well with those simulated using Cloudsat/MODIS-derived-layer optical depths.

[50] On the basis of these results, we plan to derive a new cloud climatology on the basis of OMCLDRR cloud pressures for use in future reprocessing of TOMS and OMTO3. We also plan to investigate the effects of the vertical structure of clouds on ozone and other trace retrievals. Finally, we will examine how passive instruments such as MODIS and OMI can be combined to detect the existence of multiple cloud decks and provide information on cloud vertical extents. The A-train provides a unique testbed for such studies.

[51] **Acknowledgments.** The authors thank M. Sneep and J. de Haan of KNMI for helpful comments and C. Ahn of SSAI for providing software for MODIS collocation to OMI. The material in this paper is based upon work supported by the National Aeronautics and Space Administration

(NASA) under agreement NNG06HX18C issued through the Science Mission Directorate for the EOS Aura Science Team.

References

Acarreta, J. R., J. F. de Haan, and P. Stammes (2004), Cloud pressure retrieval using the O_2-O_2 absorption band at 477 nm, *J. Geophys. Res.*, *109*, D05204, doi:10.1029/2003JD003915.

Ahmad, Z., P. K. Bhartia, and N. Krotkov (2004), Spectral properties of backscattered UV in cloudy atmospheres, *J. Geophys. Res.*, *109*, D01201, doi:10.1029/2003JD003395.

Bhartia, P. K., and C. W. Wellemeyer (2002), TOMS-V8 Total O3 Algorithm, OMI Algorithm Theoretical Basis Document, vol. 2, edited by P. K. Bhartia, Greenbelt, Md. (Available at http:/toms.gsfc.nasa.gov/version8/v8toms_atbd.pdf)

Chance, K., and R. Spurr (1997), Ring effect studies: Rayleigh scattering, including molecular parameters for rotational Raman scattering, and the Fraunhofer spectrum, *Appl. Opt.*, *36*, 5224–5230.

de Beek, R., M. Vountas, V. Rozanov, A. Richter, and J. P. Burrows (2001), The Ring effect in the cloudy atmosphere, *Geophys. Res. Lett.*, *28*, 721–724, doi:10.1029/2000GL012240.

Herman, J. R., P. K. Bhartia, O. Torres, N. C. Hsu, C. J. Seftor, and E. Celarier (1997), Global distribution of UV-absorbing aerosols from Nimbus 7/TOMS data, *J. Geophys. Res.*, *102*, 16,911–16,922, doi:10.1029/96JD03680.

Joiner, J., and P. K. Bhartia (1995), The determination of cloud pressures from rotational-Raman scattering in satellite backscatter ultraviolet measurements, *J. Geophys. Res.*, *100*, 23,019–23,026, doi:10.1029/95JD02675.

Joiner, J., and A. P. Vasilkov (2006), First results from the OMI rotational-Raman scattering cloud pressure algorithm, *IEEE Trans. Geosci. Remote Sens.*, *44*, 1272–1282, doi:10.1109/TGRS.2005.861385.

Joiner, J., P. K. Bhartia, R. P. Cebula, E. Hilsenrath, R. D. McPeters, and H. W. Park (1995), Rotational-Raman scattering (Ring effect) in satellite backscatter ultraviolet measurements, *Appl. Opt.*, *34*, 4513–4525.

Joiner, J., A. P. Vasilkov, D. E. Flittner, J. F. Gleason, and P. K. Bhartia (2004), Retrieval of cloud pressure and oceanic chlorophyll content using Raman scattering in GOME ultraviolet spectra, *J. Geophys. Res.*, *109*, D01109, doi:10.1029/2003JD003698.

Joiner, J., A. P. Vasilkov, K. Yang, and P. K. Bhartia (2006), Total column ozone over hurricanes from the Ozone Monitoring Instrument, *Geophys. Res. Lett.*, *33*, L06807, doi:10.1029/2005GL025592.

Koelemeijer, R. B. A., and P. Stammes (1999), Effects of clouds on ozone column retrieval from GOME UV measurements, *J. Geophys. Res.*, *104*, 8281–8294, doi:10.1029/1999JD900279.

Koelemeijer, R. B. A., P. Stammes, J. W. Hovenier, and J. F. de Haan (2001), A fast method for retrieval of cloud parameters using oxygen A band measurements from the GOME, *J. Geophys. Res.*, *106*, 3475–3490, doi:10.1029/2000JD900657.

Landgraf, J., O. Hasekamp, R. van Deelen, and I. Aben (2004), Rotational Raman scattering of polarized light in the Earth atmosphere: a vector radiative transfer model using the radiative transfer perturbation theory approach, *J. Quant. Spectrosc. Radiat. Transfer*, *87*, 399–433, doi:10.1016/j.jqsrt.2004.03.013.

Levelt, P. F., et al. (2006), The Ozone Monitoring Instrument, *IEEE Trans. Geosci. Remote Sens.*, *44*, 1093–1101, doi:10.1109/TGRS.2006.872333.

McPeters, R., M. Kroon, P. K. Bhartia, G. Labow, and E. Brinksma (2008), Validation of the Aura Ozone Mapping Instrument (OMI) Total Column Ozone Product, *J. Geophys. Res.*, doi:10.1029/2007JD008802, in press.

Menzel, W. P., D. P. Wylie, and K. I. Strabala (1992), Seasonal and diurnal changes in cirrus clouds as seen in four years of observations with the VAS, *J. Appl. Meteorol.*, *31*, 370–385, doi:10.1175/1520-0450(1992)031<0370:SADCIC>2.0.CO;2.

Platnick, S., M. D. King, S. A. Ackerman, W. P. Menzel, B. A. Baum, J. C. Riédi, and R. A. Frey (2003), The MODIS cloud products: algorithms and examples from Terra, *IEEE Trans. Geosci. Remote Sens.*, *41*, 459–473, doi:10.1109/TGRS.2002.808301.

Siewert, C. (2000), A concise and accurate solution to Chandrasekhar's basic problem in radiative transfer, *J. Quant. Spectrosc. Radiat. Transfer*, *64*, 109–130, doi:10.1016/S0022-4073(98)00144-7.

Sneep, M., J. F. de Haan, P. Stammes, C. Vanbauce, J. Joiner, A. P. Vasilkov, and P. F. Levelt (2008), Three way comparison between two OMI/Aura and one POLDER/PARASOL cloud pressure products, *J. Geophys. Res.*, doi:10.1029/2007JD008694, in press.

Spurr, R. (2002), Simultaneous derivation of intensities and weighting functions in a general pseudo-spherical discrete ordinate radiative transfer treatment, *J. Quant. Spectrosc. Radiat. Transfer*, *75*, 129–175, doi:10.1016/S0022-4073(01)00245-X.

Spurr, R., T. Kurosu, and K. Chance (2001), A linearized discrete ordinate radiative transfer model for atmospheric remote sensing retrieval, *J. Quant. Spectrosc. Radiat. Transfer*, *68*, 689–735, doi:10.1016/S0022-4073(00)00055-8.

Spurr, R., J. F. de Haan, R. van Oss, and A. Vasilkov (2008), Discrete ordinate radiative transfer in a stratified medium with first order rotational Raman scattering, *J. Quant. Spectrosc. Radiat. Transfer*, *109*, 404–425.

Stephens, G. L., et al. (2002), The CloudSat Mission and the A-Train: A new dimension of space-based observations of clouds and precipitation, *Bull. Am. Meteorol. Soc.*, *83*, 1771–1790, doi:10.1175/BAMS-83-12-1771.

Vasilkov, A. P., J. Joiner, J. Gleason, and P. K. Bhartia (2002), Ocean Raman scattering in satellite backscatter UV measurements, *Geophys. Res. Lett.*, *29*(17), 1837, doi:10.1029/2002GL014955.

Vasilkov, A. P., J. Joiner, K. Yang, and P. K. Bhartia (2004), Improving total column ozone retrievals by using cloud pressures derived from Raman scattering in the UV, *Geophys. Res. Lett.*, *31*, L20109, doi:10.1029/2004GL020603.

Vountas, M., V. Rozanov, and J. Burrows (1998), Ring effect: Impact of rotational Raman scattering on radiative transfer in Earth's atmosphere, *J. Quant. Spectrosc. Radiat. Transfer*, *60*, 943–961, doi:10.1016/S0022-4073(97)00186-6.

Ziemke, J. R., S. Chandra, and P. K. Bhartia (2001), "Cloud slicing": A new technique to derive upper tropospheric ozone from satellite measurements, *J. Geophys. Res.*, *106*, 9853–9867, doi:10.1029/2000JD900768.

Ziemke, J. R., S. Chandra, B. N. Duncan, L. Froidevaux, P. K. Bhartia, P. F. Levelt, and J. W. Waters (2006), Tropospheric ozone determined from Aura OMI and MLS: Evaluation of measurements and comparison with the Global Initiative's Chemical Transport Model, *J. Geophys. Res.*, *111*, D19303, doi:10.1029/2006JD007089.

P. K. Bhartia and J. Joiner, NASA/Goddard Space Flight Center, Greenbelt, MD 20771, USA.

P. Levelt, Royal Netherlands Meteorological Institute (KNMI), P.O. Box 201, NL-3730 AE De Bilt, Netherlands.

R. Spurr, RT Solutions Incorporated, Cambridge, MA 02138, USA.

G. Stephens, Colorado State University, Fort Collins, CO 80523, USA.

A. Vasilkov, Science Systems and Applications Incorporated, Lanham, MD 20706, USA. (alexander_vassilkov@ssaihq.com)